Understanding the Optical and Magnetic Properties of Ytterbium (III) Complexes

David Esteban-Gómez, Laura A. Büldt, Paulo Pérez-Lourido, Laura Valencia, Michael Seitz, and Carlos Platas-Iglesias

Inorganic Chemistry 2019 58 (6), 3732-3743
DOI: 10.1021/acs.inorgchem.8b03354

Understanding the Optical and Magnetic Properties of Ytterbium(III) Complexes

David Esteban-Gómez,[†] Laura A. Büldt,[‡] Paulo Pérez-Lourido,[§] Laura Valencia,[§] Michael Seitz,*[,‡] and Carlos Platas-Iglesias*[,†]

[†] Centro de Investigacións Científicas Avanzadas (CICA) and Departamento de Química Fundamental, Universidade da Coruña, Campus da Zapateira-Rúa da Fraga 10, 15008 A Coruña, Spain

[‡] Institute of Inorganic Chemistry, University of Tübingen, Auf der Morgenstelle 18, 72076 Tübingen, Germany

[§] Departamento de Química Inorgánica, Facultad de Ciencias, Universidade de Vigo, As Lagoas, Marcosende, 36310 Pontevedra, Spain

ABSTRACT: The absorption and emission spectra of three Yb^{3+} complexes possessing D_3, D_2 and C_2 symmetries were analyzed with the aid of ab initio calculations based on Complete Active Space Self-Consistent Field (CASSCF) wave functions (CAS(13,7)). The absorption spectra present contributions from both cold and hot bands, involving thermally populated excited sublevels of the $^2F_{7/2}$ manifold. The high-resolution emission spectrum of the tris-picolinate complex $[Yb(DPA)_3]^{3-}$ recorded at 77 K presents four components, while the complexes with macrocyclic ligands show both cold and hot emission bands, resulting in more than four components for the $^2F_{5/2}\rightarrow{}^2F_{7/2}$ transition. The combined information provided by the absorption and emission spectra allowed to identify most of the crystal field sublevels of the $^2F_{5/2}$ and $^2F_{7/2}$ states. The energies of these crystal field components are well reproduced by the ab initio calculations, with deviations typically lower than 100 cm^{-1}. The crystal field splitting is very sensitive to subtle changes of the Yb^{3+} coordination environment. The magnetic anisotropy of $[Yb(DPA)_3]^{3-}$ obtained with ab initio calculations was found to be extremely sensitive to changes in the twist angle of the upper and lower faces of the tricapped trigonal prismatic coordination polyhedron. Ab initio ligand field theory (AILFT) provides a straightforward chemical justification for the changes in magnetic anisotropy, which are responsible for the observed pseudocontact shifts in the NMR spectra.

INTRODUCTION

The coordination chemistry of the lanthanoid ions (Ln^{3+}) has been the focus of great attention in the last decades due to the fascinating magnetic and optical properties of the complexes of these ions.[1,2] The Ln^{3+} ions present rather similar chemical properties and coordination chemistry, the main differences being mainly caused by the smooth contraction of the ionic radii across the 4f period as a consequence of the lanthanoid contraction.[3] However, the magnetic and optical properties of Ln^{3+} complexes are generally related to the distribution of the 4f electrons, and therefore change dramatically depending on the specific ion. In particular, the crystal field splitting of the 4f levels is of key importance, as it determines the magnetic anisotropy of the system,[4] which in turn is responsible for the pseudocontact NMR shifts[5-7] of Ln^{3+} complexes or their single molecule magnet (SMM) behavior.[8]

Among the paramagnetic Ln^{3+} ions, Yb^{3+} presents the simplest electronic structure associated to its $4f^{13}$ configuration, which leads to a single ^2F term that splits into the $^2F_{5/2}$ and $^2F_{7/2}$ levels due to spin-orbit coupling. Crystal field effects split the $^2F_{5/2}$ and $^2F_{7/2}$ levels into three and four Kramers doublets, respectively.[9] The electronic transitions involving the $^2F_{5/2}$ and $^2F_{7/2}$ levels are observed in the NIR spectral region around 10,000 cm^{-1}. Thus, a detailed analysis of the absorption and emission spectra of Yb^{3+} complexes can potentially provide information on the coordination environment around the metal ion. The absorption spectral properties of Yb^{3+} complexes in the NIR region are also of paramount importance in the preparation of up-converting molecular systems using Yb^{3+} sensitization.[10] The pseudocontact shifts of Yb^{3+} were also widely used as a source of structural information in solution,[11] as well as to aid structure determination of complex molecules such as proteins.[12] Different Yb^{3+} complexes were also found to possess interesting SMM properties.[13]

While some pioneering studies revealed key features of the absorption and emission spectra of Yb^{3+} complexes, detailed spectral analyses which lead to a fundamental understanding of the intricacies of the electronic structure at the metal center are scarce. Perkins and Crosby reported a study of the crystal-field splitting in Yb^{3+} chelates using absorption and emission spectroscopy and crystal-field calculations.[9] The qualitative analysis of the NIR-CD spectra of chiral YbDOTA derivatives revealed that the spectra were very sensitive to the coordination polyhedron of the Yb^{3+} ion.[14] However, these studies did not reveal the

interconnection between the spectroscopic data and the geometric and electronic structure of Yb^{3+} complexes.

Herein, we present a comprehensive investigation of the details of the electronic structures via absorption and emission spectroscopy of several well-characterized Yb^{3+} complexes (Chart 1). Given the expected dependence of the crystal field splitting patterns of the $^2F_{5/2}$ and $^2F_{7/2}$ levels with the coordination environment, we selected a family of complexes possessing different structural features: The well-known $[Yb(DPA)_3]^{3-}$ complex, which presents a tricapped trigonal prismatic coordination environment (D_3 symmetry),[15-16] the ten-coordinate $[YbL^1]^{3+}$ complex,[17] which adopts D_2 symmetry in solution, and the $[Yb(Me2DO2PA)]^+$ complex (C_2 symmetry).[18] The absorption and emission spectra of these complexes are presented. A full assignment of the crystal-field components of these spectra was achieved with the use of ab initio multiconfigurational relativistic calculations based on the Complete Active Space Self-Consistent Field (CASSCF). The corresponding wave functions were analyzed using N-electron valence perturbation theory to second order (NEVPT2), while SOC effects were introduced by quasi-degenerate perturbation theory (QDPT). The CASSCF/NEVPT2/QDPT method was recently found to reproduce rather well the crystal field levels of the $[LnCl_6]^{3-}$ complexes present in elpasolite $Cs_2NaLnCl_6$ crystals.[19] The combined experimental and theoretical analysis presented in this work provides an unprecedented understanding of the electronic and optical properties of Yb^{3+} complexes, which encode information on their structure and magnetic properties.

Chart 1. Ligands discussed in the present work and numbering scheme used for the analysis of pseudocontact shifts.

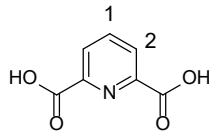

H_2DPA

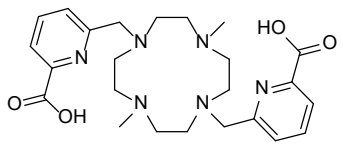

H_2Me2DO2PA

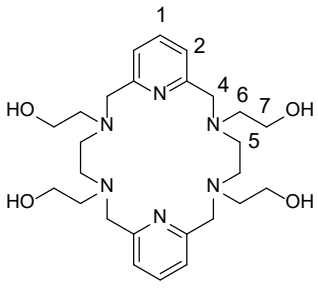

L^1

RESULTS AND DISCUSSION

Magnetic anisotropies and pseudocontact shifts. The molecular geometries of the $[Yb(Me2DO2PA)]^+$, $[YbL^1]^{3+}$ and $[Yb(DPA)_3]^{3-}$ complexes were obtained with DFT by well-established methods using the large-core approximation.[20] The $[Yb(DPA)_3]^{3-}$ complex is axially symmetric, which makes the analysis of pseudocontact shifts straightforward. The D_2 symmetry of the $[YbL^1]^{3+}$ complex does not ensure axial symmetry, but still the position of the magnetic axes should match the three perpendicular C_2 axes of the complex. Thus, we initially tested the quality of the computed geometries and the CASSCF/NEVPT2/QDPT calculations by performing a theoretical estimation of the pseudocontact shifts using the calculated magnetic susceptibilities. Indeed, calculations based on the CASSCF/RASSI/SINGLE_ANISO approach were demonstrated to provide magnetic susceptibility tensors that correlated very well with the observed pseudocontact shifts of axially symmetric complexes.[6,7] Our CASSCF/NEVPT2/QDPT calculations provide the magnetic susceptibility tensors shown in Table 1. The tensors calculated for both $[Yb(DPA)_3]^{3-}$ and $[YbL^1]^{3+}$ are diagonal, which confirms that the chosen molecular frames match the principal magnetic axes systems (Table S1, Supporting Information).[21] For $Yb(Me2DO2PA)]^+$ the molecule was orientated so that the z axis matches the C_2 symmetry axis of the complex. However, the positions of the x and y axes in the molecular susceptibility tensor are not constrained by symmetry. It turned out that the positions of the x and y axes of the susceptibility tensor are such that the angle defined by the xz plane and that delineated by the plane containing the z axis and a nitrogen atom of the macrocycle functionalized with a picolinate arm is about 35.5º (Table S1, Supporting Information). This angle deviates by ~9º with respect to that obtained previously from the analysis of the pseudocontact shifts (26.9º).[18a]

The magnetic susceptibility tensor calculated for $[Yb(DPA)_3]^{3-}$ presents a small rhombic contribution, which we attribute to the slight distortion of the D_3 symmetry of our DFT structure. Most likely dynamic effects in solution result in a free rotation of the magnetic axes in the xy plane, so that the rhombic contribution vanishes. Important rhombic contributions (~25%) were also obtained for $[Yb(DPA)_3]^{3-}$ bound to proteins.[22] The pseudocontact shifts can be expressed as linear combinations of the axial and rhombic components of the susceptibility tensor χ:[21]

$$\delta^{pc} = \frac{1}{2N_A}\left[(\chi_{zz} - \chi_{av})\left(\frac{3z^2-r^2}{r^5}\right) + (\chi_{xx} - \chi_{yy})\left(\frac{x^2-y^2}{r^5}\right)\right] \quad (1)$$

$$r = \sqrt{x^2 + y^2 + z^2} \quad (2)$$

This equation uses the Cartesian coordinates of atom i relative to the location of the paramagnetic ion, instead of the more usual spherical coordinates. For axial symmetry the rhombic term of this equation vanishes, as $(\chi_{xx} - \chi_{yy}) = 0$. The axial term value of $\chi_{zz} - \chi_{av}$ = 0.749 cm^3 K mol^{-1} obtained for $[Yb(DPA)]^{3-}$ provides pseudocontact shifts of -8.09 and -9.16 ppm for H1 and H2, respectively (see Chart 1 for labelling). These values are in good agreement with the experimental paramagnetic shifts of -6.82 and -7.75 ppm obtained by Ouali et al. using the chemical shifts of the diamagnetic Lu^{3+} complex as a reference.[15a] It must be pointed out that the paramagnetic shifts of Yb^{3+} complexes are dominated by the pseudocontact mechanism, but some small contact contributions may be present as well. Furthermore, the calculated $\chi_{zz} - \chi_{av}$ term is in nice agreement with that derived from the data of Ouali (Table 1).[15a]

Given the remarkably good theoretical prediction of the pseudocontact shifts in $[Yb(DPA)_3]^{3-}$, we next analyzed the $[YbL^1]^{3+}$ and $[Yb(Me2DO2PA)]^+$ complexes. The χ_{zz}-χ_{av} and χ_{xx}-χ_{yy} values obtained using the optimized geometries are in qualitative

agreement with the experimental data obtained from the analysis of the corresponding NMR spectra (Table 1). We attribute the relatively large deviations of the experimental and calculated data to the sensitivity of the magnetic susceptibility tensor to tiny structural changes, as proved recently by Parker.[7,23] We hypothesized that in the case of $[YbL^1]^{3+}$ the difference between the experimental and calculated magnetic susceptibilities are related to structural changes affecting the flexible hydroxyethyl pendant arms, rather than the rigid macrocyclic unit. We therefore explored the effect that changing the O-Yb-O angles α involving two hydroxyl groups coordinating from the same side of the macrocyclic plane. These angles were fixed to values in the range 59 – 71º and the structure was relaxed by geometry optimization within the D_2 point group. The corresponding χ_{zz}-χ_{av} and χ_{xx}-χ_{yy} values obtained with CASSCF/NEVPT2/QDPT calculations vary significantly as a function of α. Both the axial and rhombic magnetic susceptibilities approach the experimental values on reducing α from 71º to about 64º, while smaller angles provide calculated data with increasing deviations from the experiment (Figure 1). We next explored the effect of varying the Yb-O distances at a fixed value of α = 64.0º. Both χ_{zz}-χ_{av} and χ_{xx}-χ_{yy} change experience very important changes by varying the Yb-O distances in the range 2.426-2.474 Å. The magnetic susceptibility values calculated by using α = 64.0º and Yb-O = 2.438 Å provide an excellent agreement with the experimental data (Table 1), which is in contrast with the relatively large deviations obtained with the optimized structure (α = 67.8º and Yb-O = 2.454 Å). Furthermore, the pseudocontact shifts obtained from the CASSCF/NEVPT2/QDPT magnetic susceptibility data using the optimized geometry show rather large deviations from the experimental pseudocontact shifts. An good agreement is however observed with the susceptibility values calculated for the structure with α = 64.0º and Yb-O = 2.438 Å (Figure 2). Thus, these studies confirm that very small structural changes may have a deep impact in the magnetic anisotropy of Yb^{3+} complexes.

Table 1. Components of the magnetic susceptibility tensors (cm^3 K mol^{-1}) obtained with CASSCF/NEVPT2/QDPT calculations for different Yb^{3+} complexes.

	DPA [a]	L^1 [b]	Me2DO2PA [c]
χ_{xx}	1.917	3.342 [e] / 2.875 [f]	1.385
χ_{yy}	2.218	1.260 [e] / 1.462 [f]	4.097
χ_{zz}	3.191	2.247 [e] / 2.548 [f]	1.715
$(\chi_{zz}-\chi_{av})^{cald}$	0.749	-0.036 [e] / 0.253 [f]	-0.684
$(\chi_{zz}-\chi_{av})^{exp\ d}$	0.700	0.27	-0.041
$(\chi_{xx}-\chi_{yy})^{cald}$	-0.301	2.082[e] /1.413 [f]	2.711
$(\chi_{xx}-\chi_{yy})^{exp\ d}$	-	1.505	1.662

[a] The principle magnetic axis matches the position of the C_3 symmetry axis of the complex. All data at 298 K. [b] The magnetic axes match the three perpendicular C_2 axes of the molecule. All data at 298 K. [c] The principal magnetic axis coincides with the C_2 symmetry axis of the molecule. Experimental and calculated data obtained at 278 K. [d] Experimental values obtained from references 15a, 17a and 18a. [e] Data calculated using the optimized geometry (Yb-O 2.454 Å and O-Yb-O of 67.8º. [f] Values obtained for Yb-O = 2.438 Å and O-Yb-O = 64.0º (see text).

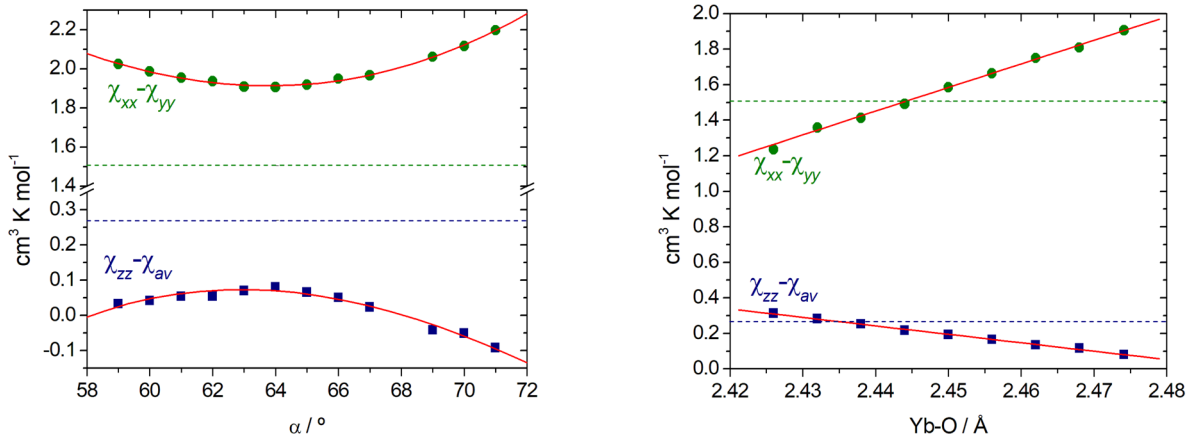

Figure 1. Axial and rhombic magnetic susceptibilities of $[Yb(L^1)]^{3+}$ as a function of the O-Yb-O angle α (left panel) and the Yb-O distance (right panel, α fixed at 64.0º) obtained with CASSCF/NEVPT2/QDPT calculations at 298 K. The dashed lines indicate the experimental χ_{zz}-χ_{av} and χ_{xx}-χ_{yy} values.

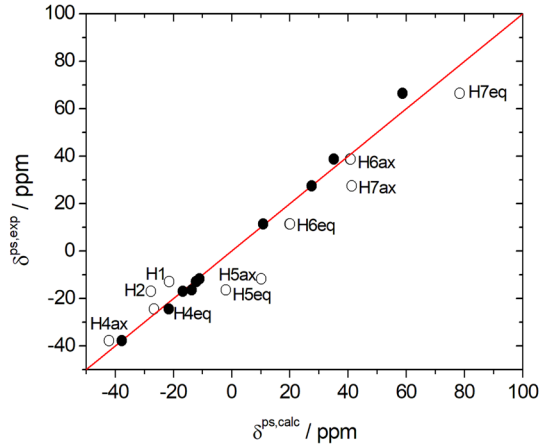

Figure 2. Plot of the experimental ^{1}H NMR pseudocontact shifts of $[Yb(L^1)]^{3+}$ versus those calculated from magnetic susceptibility data obtained with CASSCF/NEVPT2/QDPT calculations using the optimized geometry (α = 67.8º and Yb-O = 2.454 Å, open symbols, R^2 = 0.965) and the structure with α = 64.0º and Yb-O = 2.438 Å (filled symbols, R^2 = 0.998). The red line corresponds to the identity line. See Chart 1 for labelling.

Absorption spectra. Given the remarkable agreement between the experimental and calculated magnetic anisotropies of the $[Yb(DPA)_3]^{3-}$ and $[YbL^1]^{3+}$ complexes, assessed through the analysis of the corresponding pseudocontact shifts, we turned our attention to the NIR absorption spectra. The absorption spectra of the complexes recorded in D_2O solution at room temperature (CD_3OD/CD_3CD_2OD for $[Yb(DPA)_3]^{3-}$) are shown in Figure 3. All complexes show a relatively broad band envelope spanning the range 9500 - 11000 cm^{-1} that presents several components. The absorption bands are typical of the $^2F_{5/2} \leftarrow {}^2F_{7/2}$ transitions of Yb^{3+}.[9,10] For the Kramers ion Yb^{3+}, every crystal-field level is a double degenerate, so that the $^2F_{7/2}$ level splits into four doublets and the $^2F_{5/2}$ level into three doublets. The fits of the absorption spectra using a combination of Gaussian functions allowed identification of several of the components of the absorption spectra, which are listed in Table 2.

The absorption spectra of the three complexes investigated in this work show quite different shapes and absorption maxima, suggesting different crystal field splitting patterns of the $^2F_{5/2}$ and $^2F_{7/2}$ levels. For instance, the absorption spectrum of $[Yb(Me2DO2PA)]^+$ shows a maximum at 10241 cm^{-1} and a number of components on the high energy side, while the spectrum of $[YbL^1]^{3+}$ presents a maximum at 10358 cm^{-1} and several other components at lower energy (10236, 10133 and 9994 cm^{-1}). The spectrum of $[Yb(DPA)_3]^{3-}$ is dominated by a central absorption at 10186 cm^{-1} that presents two shoulders at 9866 and 10443 cm^{-1} (Figure 3).

As it has been pointed out recently, the crystal-field splitting of the $^2F_{7/2}$ term in Yb^{3+} complexes is likely comparable to kT at room temperature.[24] Indeed, early studies in Yb^{3+} tris-acetylacetonate complexes reported crystal field splitting energies of up to ~700 cm^{-1}.[9] As a result, an assignment of the different crystal-field transitions of the absorption spectra is not straightforward, as up to 12 transitions are possible if the four Kramers doublets of the $^2F_{7/2}$ level present significant populations at room temperature. Thus, we turned our attention to theory, in an attempt to identify the different crystal-field components of the absorption spectra. We therefore used ab initio CASSCF/NEVPT2/QDPT calculations to investigate the absorption spectra shown in Figure 3. The output of the calculations provided the energies of the different crystal field levels and the oscillator strengths characterizing each transition. The results are summarized in Table 2.

The comparison of the experimental and calculated spectra (Figure 3) shows that the theoretical calculations reproduce reasonably well the absorption profiles. It is also worth noting that the absorption spectra present contributions from both cold absorptions, which involve the lowest energy Kramers doublet level of the $^2F_{7/2}$ level, and hot absorptions. The presence of hot absorptions is particularly evident in the case of $[YbL^1]^{3+}$. The experimental spectrum presents absorption features at 9994, 10133, 10236 and 10424 cm^{-1} that are assigned as hot absorptions. The corresponding calculated values differ from the experimental ones only by < 35 cm^{-1} (Table 2).

Emission spectra. The emission spectra of the Yb^{3+} complexes were measured at 77 K in D_2O/glycerol (2:3, v/v) or CD_3OD/CD_3CD_2OD glassy matrixes, under excitation through the ligand bands. The emission spectrum of $[Yb(DPA)_3]^{3-}$ is particularly simple, and shows the four components associated to the $^2F_{5/2} \rightarrow {}^2F_{7/2}$ transition (Figure 4). The emission spectrum is dominated by a rather sharp component at 10222 cm^{-1} and broader peaks at 10119 and 9871 cm^{-1}, the latter with a shoulder arising from the fourth component (estimated at 9920 cm^{-1} through Gaussian deconvolution). The energies of the four transitions are predicted to a rather good accuracy by our theoretical calculations (Table 2), with deviations in the range 5-104 cm^{-1}. Thus, the emission spectrum of $[Yb(DPA)_3]^{3-}$ provides direct access to the splitting of the $^2F_{7/2}$ level (0, 103, 302 and 351 cm^{-1}). The emission spectrum recorded at room temperature (Figure S1, Supporting Information) shows broader components, and matches well that recorded in a silica-PEG hybrid matrix[25] and in acetonitrile solution.[26]

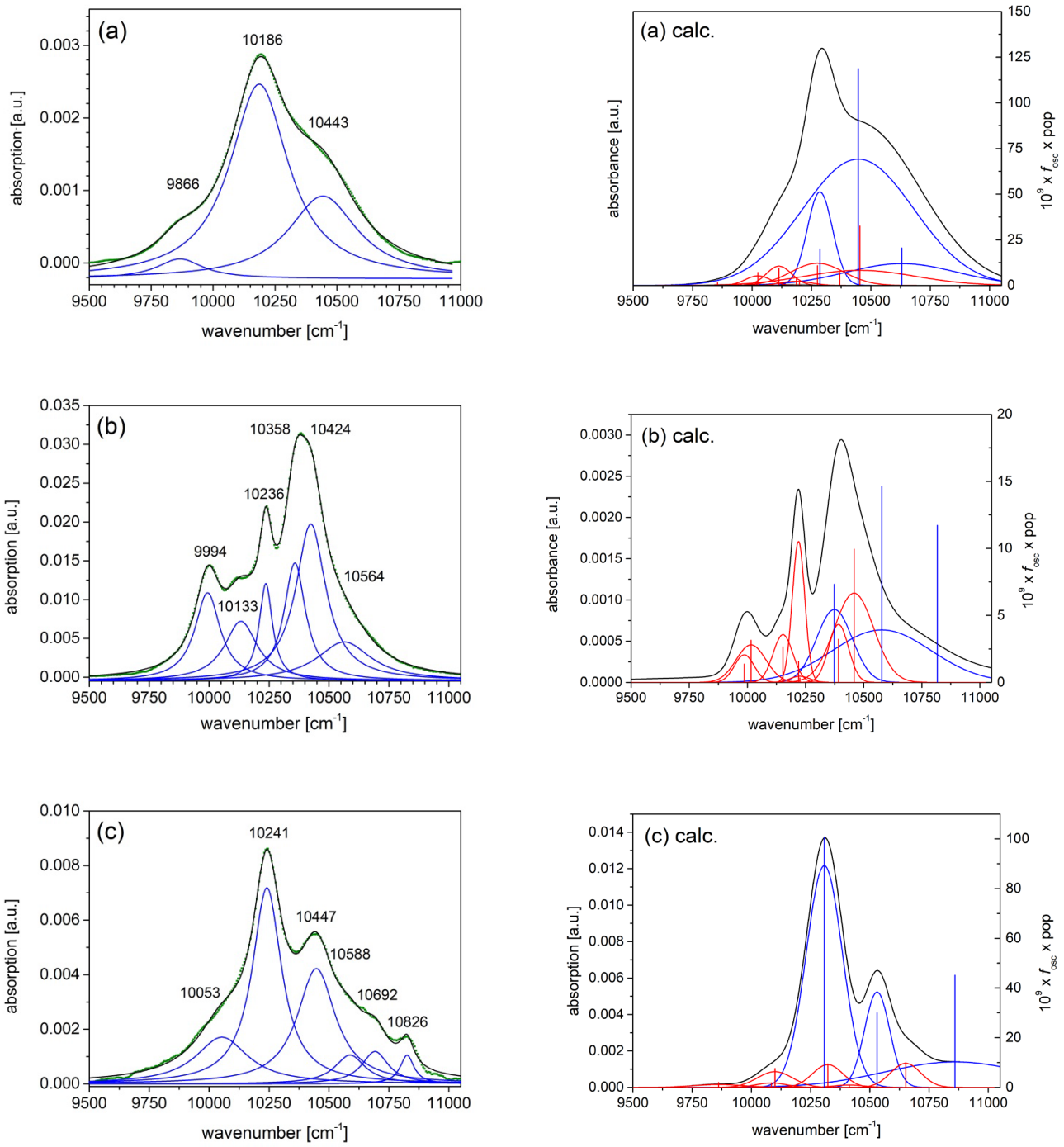

Figure 3. Left panel: NIR absorption spectra recorded from solutions of (a) $[Yb(DPA)]^{3-}$ in CD_3OD/CD_3CD_2OD, (b) $[YbL^1]^{3+}$ in D_2O, (b) and (c) $[Yb(Me2DO2PA)]^{+}$ in D_2O. The grey lines correspond to the deconvolution of the spectra using Gaussian functions. Right panel: NIR absorption spectra simulated using CASSCF/NEVPT2/QDPT calculations (black lines). The blue lines indicate cold absorptions and red lines hot absorptions. The vertical lines show the product of the oscillator strengths and the population of the ground state.

Table 2. Absorption spectral data calculated with CASSCF/NEVPT2/QDPT calculations and experimental energies obtained from absorption and emission spectroscopy.

$[YbL^1]^{3+}$	Transition (pop.)[a]	Energy (cm^{-1})	$10^9 \times f_{osc}$	Exp (absorp.)[b]	Exp (emiss.)[c]
	4←0 (0.732)	10374.0	10	10358	10357
	5←0 (0.732)	10578.1	20	10564	10553
	6←0 (0.732)	10817.0	16		
	4←1 (0.131)	10015.6	24	9994	10042
	5←1 (0.131)	10219.8	12	10236	10248
	6←1 (0.131)	10458.6	76	10424	
	4←2 (0.095)	9948.8	0	-	
	5←2 (0.095)	10152.9	28	10133	
	6←2 (0.095)	10391.8	34	-	
	4←3 (0.043)	9782.4	0	-	9837
	5←3 (0.043)	9986.5	32	-	
	6←3 (0.043)	10225.4	8	-	
$[Yb(Me2DO2PA)]^+$	Transition (pop.)	Energy (cm^{-1})	$10^9 \times f_{osc}$	Exp (absorp.)	Exp (emiss.)
	4←0 (0.654)	10308.0	154	10241	10276
	5←0 (0.654)	10530.8	46	10447	10503
	6←0 (0.654)	10860.0	69	10826	
	4←1 (0.240)	10099.5	29	10053	10026
	5←1 (0.240)	10322.4	36	-	10211
	6←1 (0.240)	10651.6	38	10692	
	4←2 (0.077)	9861.4	24	-	9743
	5←2 (0.077)	10084.3	22	-	9971
	6←2 (0.077)	10413.5	12	-	
	4←3 (0.028)	9647.4	0	-	9594
	5←3 (0.028)	9870.3	4	-	9835
	6←3 (0.028)	10199.5	4	-	10087
$[Yb(DPA)_3]^{3-}$	Transition (pop.)	Energy (cm^{-1})	$10^9 \times f_{osc}$	Exp (absorp.)	Exp (emiss.)
	4←0 (0.540)	10285.6	37	10186	10222
	5←0 (0.540)	10447.2	220	10443	
	6←0 (0.540)	10630.2	38		
	4←1 (0.236)	10113.5	40		10119
	5←1 (0.236)	10275.1	46		
	6←1 (0.236)	10454.1	138		
	4←2 (0.155)	10024.8	46		9920
	5←2 (0.155)	10186.3	24		
	6←2 (0.155)	10369.4	46		
	4←3 (0.068)	9854.9	22	9866	9871
	5←3 (0.068)	10016.4	20		
	6←3 (0.068)	10199.5	32		

[a] Values within parentheses correspond to the Boltzmann populations of the lowest energy level involved in the transition at 300 K. [b] Experimental data obtained from the analysis of the absorption spectra. [c] Experimental data obtained from emission spectra.

The emission spectrum obtained for $[YbL^1]^{3+}$ is more complex, showing a maximum at 10042 cm^{-1} and up to four additional transitions that could be identified by spectral deconvolution (Figure 5). This is surprising at first sight, given the presence of a single complex species in solution evidenced by NMR spectroscopy.[17] Thus, we hypothesized that some of the transitions observed in the emission spectra are related to hot bands, as suggested previously for Yb^{3+} porphyrins.[27] The inspection of the experimental and calculated data allowed us to assign the components at 9837, 10042 and 10357 cm^{-1} as cold emission bands, while the rather sharp component at 10248 cm^{-1} and the broad feature at 10553 cm^{-1} can be attributed to hot

bands, arising from thermally populated excited (sub)states. The emission spectrum recorded at room temperature presents essentially the same features (Figure S2, Supporting Information), except for the component at ca. 10500 cm^{-1}. This component is already rather broad at 77 K and it is not observed at room temperature probably because of extreme broadening. The intensity of the emission peak at 10210 cm^{-1} in the spectrum recorded at room temperature clearly increases in intensity with respect to the components at 9837 and 10042 cm^{-1}, when compared to the analogous features in the spectrum recorded at low temperature. This supports the assignment of the maximum at 10248 cm^{-1} in the spectrum recorded at low temperature as a hot band (10210 cm^{-1} at room temperature). Some weak components in the emission spectra of Yb^{3+}-doped crystals were assigned as vibronic bands.[28] However, the 4f orbitals are well shielded from the surroundings by the outer 5p orbitals, so that vibronic bands are generally not observed for Yb^{3+} complexes in solution.[27]

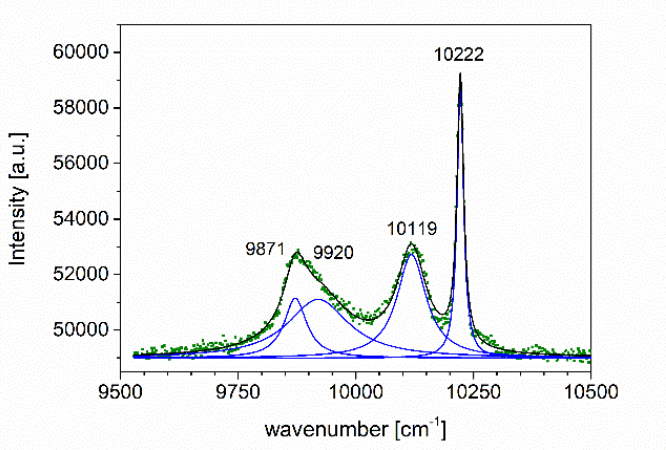

Figure 4. High-resolution luminescence spectrum (green points) of $[Yb(DPA)_3]^{3-}$ in the region of the $^2F_{5/2} \rightarrow {}^2F_{7/2}$ transition (in glassy matrix CD_3OD/CD_3CD_2OD, T = 77 K, λ_{exc} = 260 nm, emission slits 1.5 nm) with corresponding cumulative fit function (black, individual fit components in blue).

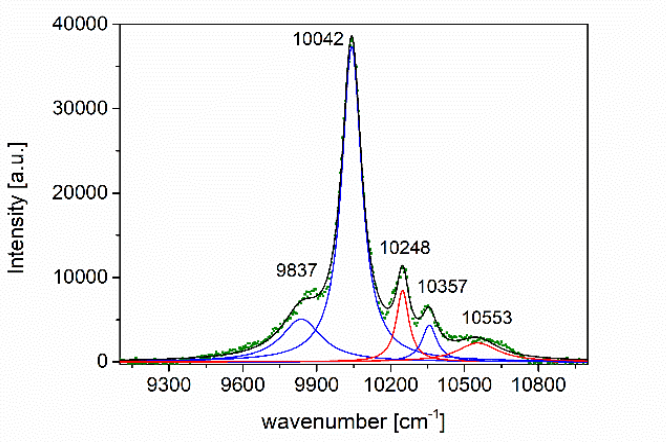

Figure 5. High-resolution luminescence spectrum (green points) of $[YbL^1]^{3+}$ in the region of the $^2F_{5/2} \rightarrow {}^2F_{7/2}$ transition (in glassy matrix D_2O/glycerol, 2:3, v/v, T = 77 K, λ_{exc} = 275 nm, emission slits 4 nm) with corresponding cumulative fit function (black, individual fit components in blue for cold bands and red for hot bands).

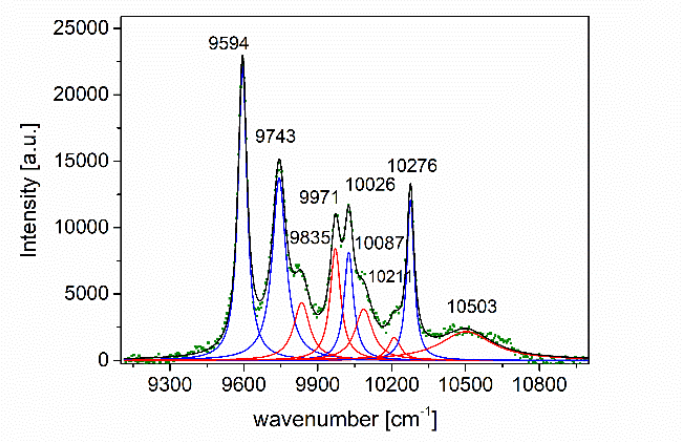

Figure 6. High-resolution luminescence spectrum (green points) of $[Yb(Me2DO2PA)]^+$ in the region of the $^2F_{5/2} \rightarrow {}^2F_{7/2}$ transition (in glassy matrix D_2O/glycerol, 2:3, v/v, T = 77 K, λ_{exc} = 275 nm, emission slits 3 nm) with corresponding cumulative fit function (black, individual fit components in blue for cold bands and red for hot bands).

The high-resolution emission spectrum recorded for $[Yb(Me2DO2PA)]^+$ shows a rather large number of components (Figure 6). Spectral deconvolution allowed us to identify nine of the maximum number of twelve components (four cold bands and eight hot bands). Ignoring the shoulder at 10087 cm^{-1}, the overall spectrum can be seen as a superposition of two emission spectra with four components each. The separation between the cold and hot components at higher energy (9594 and 9835 cm^{-1}, respectively) amounts to 240 cm^{-1}. The remaining pairs of cold and hot components present similar energy differences (~230 cm^{-1}). This is a solid proof that the emission spectrum presents bands arising not only from the lowest sub-level of the $^2F_{5/2}$ excited state, but also from higher-energy sub-levels. Furthermore, the splitting of the two lowest-energy Kramers doublets of the $^2F_{5/2}$ level obtained with CASSCF/NEVPT2/QDPT amounts to 223 cm^{-1} (Table 2), a value that is in good agreement with one deduced from the emission spectrum. The spectrum recorded at room temperature shows essentially the same features, but with broader components, indicating the ligand field splitting does not change significantly with temperature (Figure S3, Supporting Information).

The presence of hot bands in the emission spectra of $[YbL^1]^{3+}$ and $[Yb(Me2DO2PA)]^+$ is in clear contrast with the simple emission pattern observed for $[Yb(DPA)_3]^{3-}$. These results suggest that in the former two examples vibrational relaxation of the middle and upper components of the $^2F_{5/2}$ excited state are slow compared to the lifetime of the $^2F_{5/2}$ state.[29] While we do not have a definite explanation for this behavior, we hypothesize that it could be related to the more rigid structure of the complexes with macrocyclic systems.

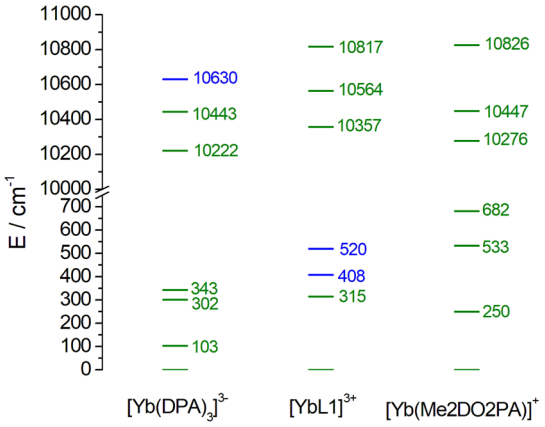

Figure 7. Energy diagram showing the splitting of the $^2F_{5/2}$ and $^2F_{7/2}$ levels by effect of the crystal-field. Each horizontal line represents a Kramers doublet. Green lines denote levels identified from the analysis of absorption and emission spectra, while blue lines indicate data obtained with CASSCF/NEVPT2/QDPT calculations.

Crystal-field splitting of the $^2F_{5/2}$ and $^2F_{7/2}$ levels. The combined analysis of the absorption and emission spectra allowed us to identify most of the sub-levels of the $^2F_{5/2}$ and $^2F_{7/2}$ levels (Figure 7). The splitting caused by the ligand-field is in the order of a few hundred cm^{-1} for all the three complexes investigated here. Both the $^2F_{5/2}$ and $^2F_{7/2}$ levels present rather different splitting patterns, with the size of the splitting increasing following the order $[Yb(DPA)_3]^{3-}$ < $[YbL^1]^{3+}$ < $[Yb(Me2DO2PA)]^+$. This effect is particularly evident for the $^2F_{7/2}$ level.

We have selected the $[Yb(DPA)_3]^{3-}$ complex to perform a more detailed investigation of the effect that subtle structural changes have on the energies of the Kramers doublets. The optimized structure of the complex shows a nearly undistorted D_3 symmetry with Yb-N and Yb-O distances of 2.506 and 2.402 Å. These values are in excellent agreement with those observed in the solid state structure (ca. 2.46 and 2.37 Å, respectively).[30] The coordination polyhedron can be described as a tricapped trigonal prism where the upper and lower tripods are defined by oxygen donor atoms and the capping tripod is described by the three N atoms. The upper and lower tripods are rotated by an angle ϕ = 11.8º. We thus generated two sets of geometries by varying the Yb-N distances in steps of 0.1 Å from 2.45 to 2.55 Å and the twist angle ϕ from ca. 0 to 20º. These geometries were generated by constraining the structures to the D_3 point group and without relaxing the geometries of the DPA^{2-} ligands. Subsequently, CASSCF/NEVPT2/QDPT calculations were run to calculate the energies of the $^2F_{5/2}$ and $^2F_{7/2}$ sublevels. The variation of the bond distances produced negligible changes on the energies of the Kramers doublets (< 14 cm^{-1}). On the contrary, the variation of the twist angle ϕ provokes dramatic effects, as shown in Figure 8. The energy separation between the ground and the excited Kramers doublets of the J = 7/2 ground term decreases by up to 500 cm^{-1} on increasing ϕ from 0 to ca. 14º. Similarly, the Kramers doublets of the J = 5/2 term experience a dramatic stabilization with respect to the ground energy term (up to 660 cm^{-1}). These results show that the splitting of the $^2F_{5/2}$ and $^2F_{7/2}$ sublevels is very sensitive to variations of the coordination environment around the Yb^{3+} ion. These results are in line with those reported recently by Parker, which demonstrated that subtle structural changes provoked dramatic effects in the crystal field splitting of C_3 symmetric Dy^{3+} complexes.[7]

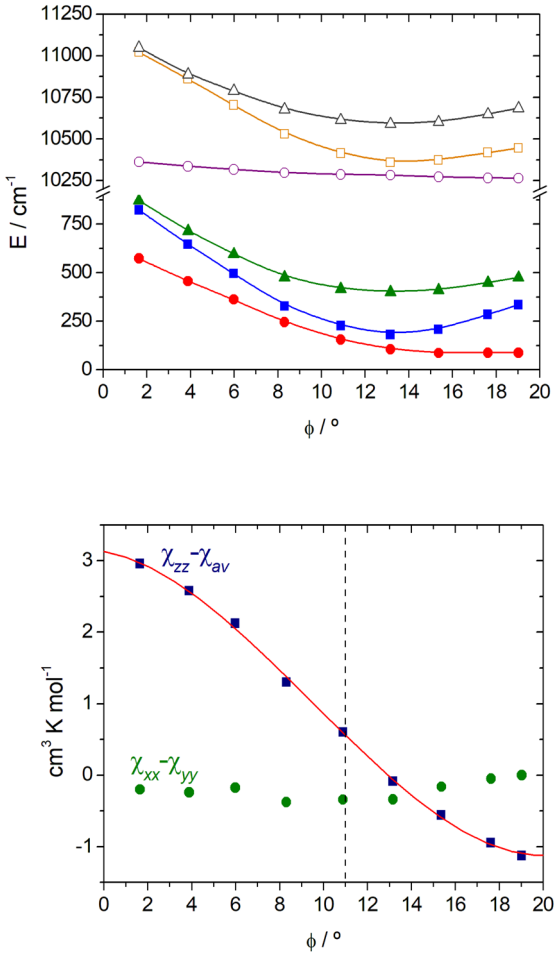

Figure 8. Top: Energies of the Kramers doublets of $[Yb(DPA)_3]^{3-}$ as a function of the twist angle ϕ. Bottom: Axial and rhombic magnetic susceptibilities of $[Yb(DPA)_3]^{3-}$ as a function of the twist angle ϕ. The dashed line corresponds to the twist angle that matches the experimental value of χ_{zz} - χ_{av}. All data obtained with CASSCF/NEVPT2/QDPT calculations at 298 K.

The axial component of the magnetic susceptibility tensor was also found to be very sensitive to the twist angle (Figure 8). The calculated χ_{zz} - χ_{av} values vary from ~3 cm^3 K mol^{-1} for twist angle of 0º to 0.0 cm^3 K mol^{-1} for ϕ = 13.0º, and then changes sign to reach χ_{zz} - χ_{av} = -1.1 cm^3 K mol^{-1} for ϕ = 19.0º, which implies that the susceptibility anisotropy switches from easy axis to easy plane by changing ϕ. The twist angle that provides the best agreement with the experimental value of χ_{zz} - χ_{av} = 0.7 cm^3 K mol^{-1} is ϕ = 10.5º, which is very close to that obtained for the equilibrium geometry (ϕ = 11.8º). These results show that the magnetic anisotropy, and thus the

pseudocontact shifts are extremely sensitive to very small structural variations.

Ab initio crystal-field analysis. In a recent work Parker et al. predicted change in sign of the magnetic susceptibility in tricapped trigonal prismatic Dy^{3+} complexes by introducing distortions in the coordination polyhedron.[7] In another recent work, a very small magnetic susceptibility was reported for an Yb^{3+} complex showing this coordination environment ($\chi_{zz} - \chi_{av} = 0.34$ cm^3 K mol^{-1}), which was reflected in very small pseudocontact shifts (< ~20 ppm).[31] Most likely the latter system presents a ϕ angle close to ~13º at which the sign of the magnetic susceptibility is reversed. Close to this ϕ value the magnetic susceptibility is expected to be nearly isotropic, so the pseudocontact shifts must be negligible. Thus, the trend predicted in Figure 8 for the $\chi_{zz} - \chi_{av}$ values of $[Yb(DPA)_3]^{3-}$ appears to represent a rather general effect in lanthanide complexes having tricapped trigonal prismatic coordination, in the sense that the magnetic anisotropy is likely changing sign as a function of the twist angle. Given the relevance of this coordination polyhedron in the coordination chemistry of the Ln^{3+} ions,[32] we sought to rationalize the magnetic anisotropy of the $[Yb(DPA)_3]^{3-}$ complex using ab initio ligand-field theory (AILFT).[33] Following the methodology developed by Atanasov,[34] the AILFT procedure provides the best least-squares fit between the pure f-orbitals assumed by crystal field theory and the predominantly f-orbitals of the complete active space [CAS(13,7) in the present case]. The results of the fit yield the 28 ligand field parameters (one for every pair of 4f orbitals), the Racah parameters and the spin orbit coupling parameter ξ.

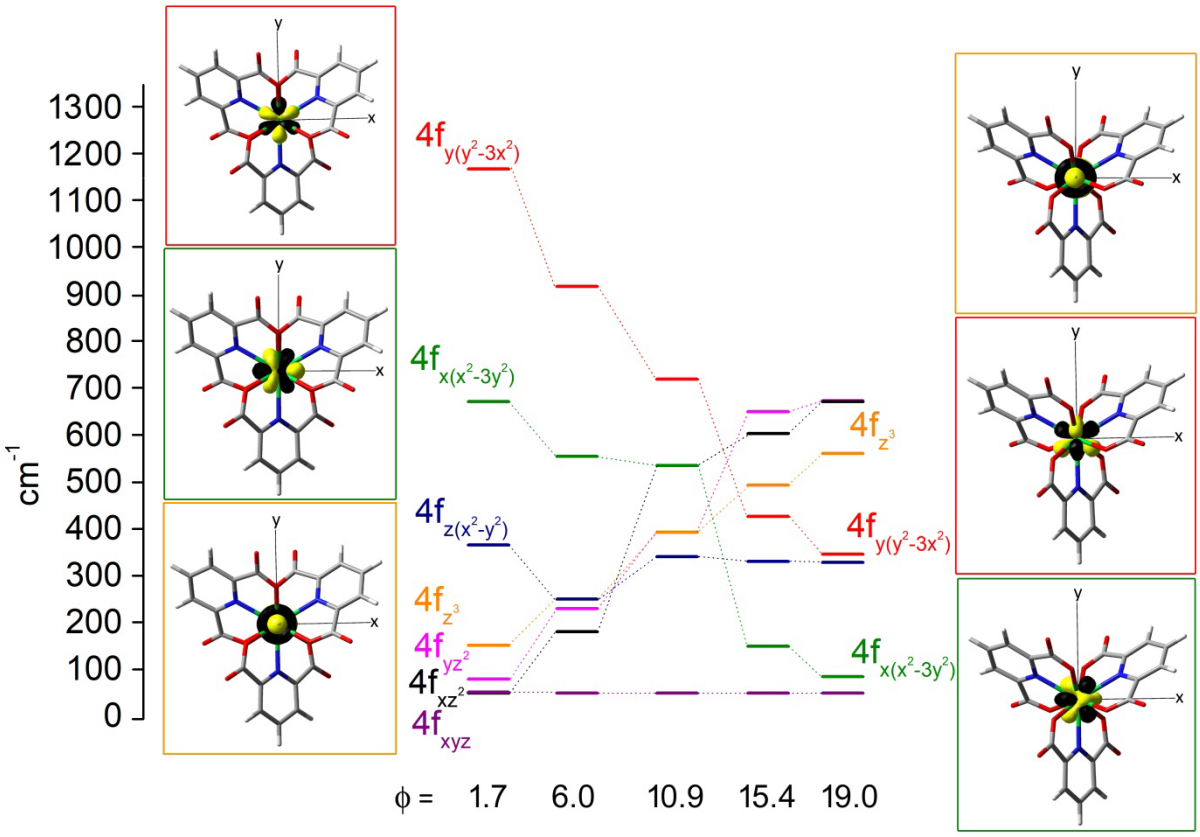

Figure 9. Splitting of the 4f orbitals obtained with AILFT for $[Yb(DPA)_3]^{3-}$ as a function of the twist angle ϕ and views of selected orbitals.

Figure 9 presents the energies of the 4f orbitals of $[Yb(DPA)_3]^{3-}$ obtained with AILFT as a function of the twist angle ϕ. For small values of ϕ, the $f_{y(y^2-3x^2)}$ orbital presents the highest energy. This is related to the 120º orientation of three of the lobes of the orbital, which point directly along the three planes defined by a C_2 symmetry axes and the z axis, and contain N and O atoms of the DPA units. The remaining three lobes of the orbital are directed along the planes containing the O atoms of the ligand. Below is the $f_{x(x^2-3y^2)}$ orbital, with lobes directed in between the C_2 symmetry axes of the molecule. The remaining five 4f orbitals present considerably lower energy, with the f_{xyz} orbital being the lowest energy one. Increasing the twist angle does not affect significantly the energy of the $f_{z(x^2-y^2)}$ orbital with respect to f_{xyz}. At fixed Yb-O distances (2.404 Å in the present case), the O atoms of the carboxylate groups

approach the *z* axis as ϕ increases. As a result, the energies of the orbitals directed along the z axis f_{xz^2}, f_{yz^2} and f_{z^3} increase in energy as the twist angle increases. Simultaneously, the orbitals with lobes oriented along the xy plane $f_{y(y^2-3x^2)}$ and $f_{x(x^2-3y^2)}$ decrease in energy. Thus, the change in sign of the magnetic susceptibility presented in Figure 8 can be rationalized by a change of the electron distribution, as a consequence of the approximation of the O donor atoms to the *z* axis upon increasing ϕ. This shifts electron density from orbitals directed along the z axis to orbitals directed on the xy plane. This has been described by Faulkner as a change from a prolate to an oblate electron distribution, which was induced by coordination of fluoride along the z axis of the complex.[6]

CONCLUSIONS

In this contribution we have selected three Yb^{3+} complexes with different symmetries of the coordination environments and analyzed the crystal field splitting of the $^2F_{5/2}$ and $^2F_{7/2}$ levels using both absorption and emission spectroscopy. The analysis of the electronic spectra was aided by post-Hartree-Fock calculations based on multiconfigurational complete-active-space self-consistent field wave functions. The application of this type of calculations to practically relevant systems has become feasible in the last years,[6,7,35] providing the opportunity to analyze the electronic structure of lanthanide complexes with an unprecedented accuracy. This study demonstrates that the electronic structure of Yb^{3+} complexes can be analyzed and understood to a great degree of detail with the assistance of advanced computational methods.

The NIR absorption spectra of the Yb^{3+} complexes presented in this work present contributions from both cold and hot absorptions, with the latter dominating the absorption profile of $[YbL^1]^{3+}$. Similarly, only the $[Yb(DPA)_3]^{3-}$ complex presents a simple four-line emission spectrum at low temperature, with $[YbL^1]^{3+}$ and $[Yb(Me2DO2PA)]^+$ presenting both cold and hot emission bands. CASSCF/NEVPT2/QDPT calculations provide a very accurate description of the crystal field splitting of the $^2F_{5/2}$ and $^2F_{7/2}$ sublevels, which is very sensitive to the geometry of the metal coordination environment. The satisfactory prediction of the crystal field splitting in these complexes indicates that the structural models used for ab initio calculations provide a good description of the solution structures, as the magnetic anisotropy of Yb^{3+} complexes was shown to be very sensitive to small structural changes, for instance provoked by a different solvent polarity.[23] The results and the methodology reported here open new avenues for the rationalization and prediction of very important properties of Yb^{3+} and other lanthanide complexes, including paramagnetic NMR shifts, magnetic anisotropies and optical spectra. These properties are of key importance to develop shift reagents or molecular systems with improved SMM or up-conversion behavior. The application of AILFT allows rationalizing magnetic anisotropy on the basis of simple chemical principles, paving the way for the prediction of this important property and the design of molecular systems with predetermined properties.

EXPERIMENTAL AND COMPUTATIONAL SECTION

Materials. $Cs_3[Yb(DPA)_3]\cdot 6H_2O$,[22] $[YbL^1](NO_3)_3\cdot 6H_2O$[17] and $[Yb(Me2DO2PA)]Cl$[18] were synthesized according to published procedures.

Near-IR absorption spectra. Near-IR absorption spectra were measured at room temperature (T = 293 K) using a JASCO V-770 spectrophotometer. The spectra were recorded in quartz cuvettes (path length: 10 mm) in the solvents indicated. The spectra were corrected for baseline drift by spline-interpolation with Origin 9.0. The component peaks of the spectra were deconvoluted by fitting of the spectra with a series of Lorentzian functions (Levenberg-Marquardt on χ^2).

Luminescence spectroscopy. Steady state near-IR emission spectra at room temperature were acquired on a Horiba Fluorolog-3 DF spectrofluorimeter using quartz cuvettes (path length: 10 mm) at room temperature. The excitation light source was a 450 W continuous xenon lamp. Emission was monitored at 90° using a Hamamatsu R2658P PMT. Spectral selection was achieved by double-grating DFM/DFX monochromators (focal lengths 2 × 300 mm, excitation grating: 1200 grooves/mm, blazed at 330 nm; emission grating: 600 grooves/mm, blazed at 1000 nm). Low temperature spectra were recorded on frozen glasses of solutions in standard NMR tubes as indicated (either D_2O/glycerol 2:3, v/v, or CD_3OD/CD_3CD_2OD 1:1, v/v) using a dewar cuvette filled with liquid N_2 (T = 77 K). The component peaks of the spectra were deconvoluted by fitting of the spectra with a series of Lorentzian functions (Levenberg-Marquardt on χ^2).

Computational details. Geometry optimizations of the $[Yb(Me2DO2PA)]^+$, $[YbL^1]^{3+}$ and $[Yb(DPA)]^{3-}$ systems were performed with the Gaussian 09 package (Revision E.01).[36] In these calculations we used the hybrid meta-GGA approximation to DFT with the TPSSh exchange-correlation functional.[37] The large-core quasi-relativistic effective core potentials (ECPs) and associated [5s4p3d]-GTO basis sets of Dolg and co. were used for Yb (59 electrons in the core),[38] while the ligand atoms were described using the standard 6-31G(d,p) basis set. Analytical frequency calculations were used to confirm that the stationary points found on the potential energy surfaces represent true energy minima.

Complete Active Space Self-Consistent Field (CASSCF)[39] and N-electron valence perturbation theory to second order (NEVPT2)[40] calculations were performed using the ORCA program package (Release 4.0.1.2).[41] Relativistic effects were considered by using the all-electron second order Douglas-Kroll-Hess (DKH2) method.[42] The SARC2-DKH-QZVP[43] basis set was used for Yb, while the DKH-def2-TZVP basis set was used for C, H, N and O. The latter basis set contains the exponents from the def2-TZVP basis set of Ahlrichs[44] and was recontracted for DKH2 calculations by D. A. Pantazis.[45] The RIJCOSX approximation[46] was used to speed up calculations using the SARC2-DKH-QZVP/JK[43] auxiliary basis set for Yb and auxiliary basis sets for the remaining atoms generated automatically by ORCA using AutoAux procedure.[47] CASSCF calculations were performed by using an active space including thirteen electrons distributed into the seven Yb 4f-based molecular orbitals (CAS(13,7)). NEVPT2 calculations were performed on the top of the CASSCF wave functions to account for dynamic correlation, while SOC effects were introduced by quasi-degenerate perturbation theory (QDPT).[48] Solvent effects were introduced with the universal solvation model based on solute

electron density and on a continuum model (SMD).[49] AILFT calculations were carried out with the ORCA program package.[33,34]

The absorption profiles were simulated from the NEVPT2 calculations by using a combination of Gaussian functions centered at the calculated excitation energies, with areas proportional to the corresponding oscillator strength (f_i) weighed by the Boltzmann population (p_i) at 300 K:[50]

$$A(E) = \sum_i a_i \exp\left(-2.773(E - E_i)^2/\Delta_{1/2}^2\right) \quad (3)$$

$$a_i = 2.174 \times 10^9 f_i p_i/\Delta_{1/2} \quad (4)$$

Where E_i is the calculated excitation energy for transition i and $\Delta_{1/2}$ is the bandwidth at half-height. The linewidths were varied by visual comparison of the experimental and calculated absorption profiles (75-400 cm-1) until a satisfactory agreement was obtained.

ASSOCIATED CONTENT

Emission spectra, views of the f orbitals, optimized Cartesian coordinates obtained with DFT, sample ORCA input file, and complete reference 35. This material is available free of charge via the Internet at http://pubs.acs.org.

AUTHOR INFORMATION

Corresponding Authors

*E-mail: carlos.platas.iglesias@udc.es (C. P.-I)
*E-mail: michael.seitz@uni-tuebingen.de (M. S.)

Author Contributions

The manuscript was written through contributions of all authors. All authors have given approval to the final version of the manuscript.

ACKNOWLEDGMENT

Authors C. P.-I. and D. E.-G. thank Ministerio de Economía y Competitividad (CTQ2016-76756-P) and Xunta de Galicia (ED431B 2017/59 and ED431D 2017/01) for generous financial support and Centro de Supercomputación of Galicia (CESGA) for providing the computer facilities. Financial support is also gratefully acknowledged from: German Research Foundation (M.S.: research grants SE 1448/6-1 and SE 1448/8-1) and University of Tübingen (L.A.B.: Athene program, Institutional Strategy (ZUK 63).

REFERENCES

(1) (a) Bünzli, J.-C. G. Lanthanide Luminescence for Biomedical Analyses and Imaging. *Chem. Rev.* **2010**, *110*, 2729-2755. (b) Law, G.-L.; Pham, T. A.; Xu, J.; Raymond, K. N. A Single Sensitizer for the Excitation of Visible and NIR Lanthanide Emitters in Water with High Quantum Yields. *Angew. Chem. Int. Ed.* **2012**, *51*, 2371-2374. (c) Martinic, I.; Eliseeva, S. V.; Nguyen, T. N.; Foucher, F.; Gosset, D.; Westall, F.; Pecoraro, V. L.; Petoud, S. Near-Infrared Luminescent Metallacrowns for Combined in vitro cell Fixation and Counter Staining. *Chem. Sci.* **2017**, *8*, 6042-6050. (d) Xu, J.; Corneillie, T. M.; Moore, E. G.; Law, G.-L.; Butlin, N. G.; Raymond, K. N. Octadentate Cages of Tb(III) 2-Hydroxyisophthalamides: A New Standard for Luminescent Lanthanide Labels. *J. Am. Chem. Soc.* **2011**, *133*, 19900-19910. (e) Heffern, M. C.; Matosziuk, L. M.; Meade, T. J. Lanthanide Probes for Bioresponsive Imaging. *Chem. Rev.* **2014**, *114*, 4496-4539. (f) Bui, A. T.; Roux, A.; Grichine, A.; Duperray, A.; Andraud, C.; Maury, O. Twisted Charge-Transfer Antennae for Ultra-Bright Terbium(III) and Dysprosium(III) Bioprobes. *Chem. Eur. J.* **2018**, *24*, 3408-3412. (g) Frawley, A. T.; Linford, H. V.; Starck, M.; Pal, R.; Parker, D. Enantioselective cellular localisation of europium(III) coordination complexes. *Chem. Sci.* **2018**, *9*, 1042-1049.

(2) (a) Liu, J.; Chen, Y.-C.; Liu, J.-L.; Vieru, V.; Ungur, L.; Jia, J.-H.; Chibotaru, L. F.; Lan, Y.; Wernsdorfer, W.; Gao, S.; Chen, X.-M.; Tong, M.-L. A Stable Pentagonal Bipyramidal Dy(III) Single-Ion Magnet with a Record Magnetization Reversal Barrier over 1000 K. *J. Am. Chem. Soc.* **2016**, *138*, 5441-5450. (b) Fatila, E. M.; Rouzieres, M.; Jennings, M. C.; Lough, A. J.; Clerac, R.; Preuss, K. E. Fine-Tuning the Single-Molecule Magnet Properties of a [Dy(III)-Radical]2 Pair. *J. Am. Chem. Soc.* **2013**, *135*, 9596-9599.

(3) Seitz, M.; Oliver, A. G.; Raymond, K. N. The Lanthanide Contraction Revisited. *J. Am. Chem. Soc.* **2007**, *129*, 11153-11160.

(4) (a) Gómez-Coca, S.; Aravena, D.; Morales, R.; Ruiz, E. Large magnetic anisotropy in Mononuclear Metal Complexes. *Coord. Chem. Rev.* **2015**, *289-290*, 379-392. (b) Zhu, Z.; Guo, M.; Li, X.-L.; Tang, J. Molecular Magnetism of Lanthanide: Advances and Perspectives. *Coord. Chem. Rev.* **2019**, *378*, 350-364. (c) Meng, Y.-S.; Jiang, S.-D.; Wang, B.-W.; Gao, S. Understanding the Magnetic Anisotropy toward Single-Ion Magnets. *Acc. Chem. Res.* **2016**, *49*, 2381-2389.

(5) Piguet, C.; Geraldes, C. Paramagnetic NMR Lanthanide Induced Shifts for Extracting Solution Structures. In Handbook on the Physics and Chemistry of Rare Earths, Vol. 33; Gschneidner, K. A., Bunzli, J.-C., Pecharsky, V., Eds.; Elsevier: Amsterdam, 2003; pp 353−463.

(6) (a) Blackburn, O. A.; Chilton. N. F.; Keller, K.; Tait, C. E.; Myers, W. K.; McInnes, E. J. L.; Kenwright, A. M.; Beer, P. D.; Timmel, C. R.; Faulkner, S. Spectroscopic and Crystal Field Consequences of Fluoride Binding by $[Yb{\cdot}DTMA]^{3+}$ in Aqueous Solution. *Angew. Chem. Int. Ed.* **2015**, *54*, 10783-10786. (b) Blackburn, O. A.; Kenwright, A. M.; Beer, P. D.; Faulkner, S. Axial fluoride binding by lanthanide DTMA complexes alters the local crystal field, resulting in dramatic spectroscopic changes. *Dalton Trans.* **2015**, *44*, 19509-19517.

(7) (a) Vonci, M.; Mason, K.; Suturina, E. A.; Frawley, A. T.; Worswick, S. G.; Kuprov, I.; Parker, D.; McInnes, E. J. L.; Chilton, N. F. Rationalization of Anomalous Pseudocontact Shifts and Their Solvent Dependence in a Series of C_3-Symmetric Lanthanide Complexes. *J. Am. Chem. Soc.* **2017**, *139*, 14166-14172. (b) Suturina, E. A.; Mason, K.; Geraldes, C. F. G. C.; Kuprov, I.; Parker, D. Beyond Bleaney's Theory: Experimental and Theoretical Analysis of Periodic Trends in Lanthanide-Induced Chemical Shift. *Angew. Chem. Int. Ed.* **2017**, *56*, 12215-12218.

(8) (a) Wang, M.; Meng, X.; Song, F.; He, Y.; Shi, W.; Gao, H.; Tang, J.; Peng, C. Reversible Structural Transformation Induced Switchable Single-Molecule Magnet Behavior in Lanthanide Metal-Organic Frameworks. *Chem. Commun.* **2018**, *54*, 10183-10186. (b) Huang, X.-D.; Xu, Y.; Fan, K.; Bao, S.-S.; Kurmoo, M.; Zheng, L.-M. Reversible SC-SC Transformation involving [4+4] Cycloaddition of Anthracene: A Single-Ion to Single-Molecule Magnet and Yellow-Green to Blue-White Emission. *Angew. Chem. Int. Ed.* **2018**, *57*, 8577-8581. (c) Latendresse, T. P.; Bhuvanesh, N. S.; Nippe, M. Hard Single-Molecule Magnet Behavior by a Linear Trinuclear Lanthanide-[1]Metallocenophane Complex. *J. Am. Chem. Soc.* **2017**, *139*, 14877-14880. (d) Ferbinteanu, M.; Kajiwara, T.; Choi, K.-Y.; Nojiri, H.; Nakamoto, A.; Kojima, N.; Cimpoesu, F.; Fujimura, Y.; Takaishi, S.; Yamashita, M. A Binuclear Fe(III)Dy(III) Single Molecule Magnet. Quantum Effects and Models. *J. Am. Chem. Soc.* **2006**, *128*, 9008-9009.

(9) Perkins, W. G.; Crosby, G. A. Crystal-Field Splitting in Yb^{3+} Chelates. *J. Chem. Phys.* **1965**, *42*, 407-414.

(10) Souri, N.; Tian, P.; Platas-Iglesias, C.; Wong, K.-L.; Nonat, A.; Charbonnière, L. J. Upconverted Photosensitization of Tb Visible Emission by NIR Yb Excitation in Discrete Supramolecular Heteropolynuclear Complexes. *J. Am. Chem. Soc.* **2017**, *139*, 1456-1459.

(11) (a) Doffek, C.; Alzakhem, N.; Bischof, C.; Wahsner, J.; Güden-Silber, T.; Lügger, J.; Platas-Iglesias, C.; Seitz, M. Understanding the Quenching Effects of Aromatic C−H- and C−D Oscillators in

Near-IR Lanthanoid Luminescence. *J. Am. Chem. Soc.* **2012**, *134*, 16413 – 16423. (b) Zhang, L.; Martins, A. E.; Zhao, P.; Tieu, M.; Esteban-Gómez, D.; McCandless, G. T.; Platas-Iglesias, C.; Sherry, A. D. Enantiomeric Recognition of D- and L-Lactate by CEST with the Aid of a Paramagnetic Shift Reagent. *J. Am. Chem. Soc.* **2017**, *139*, 17431-17437. (c) Vipond, J.; Woods, M.; Zhao, P.; Tircso, G.; Ren, J.; Bott, S. G.; Ogrin, D.; Kiefer, G. E.; Kovacs, Z.; Sherry, A. D. A Bridge to Coordination Isomer Selection in Lanthanide(III) DOTA-tetraamide Complexes. *Inorg. Chem.* **2007**, *46*, 2584-2595.

(12) (a) Bertini, I.; Lanik, M. B. L.; Lee, Y.-M.; Luchinat, C.; Rosato, A. Magnetic Susceptibility Tensor Anisotropies for a Lanthanide Ion Series in a Fixed Protein Matrix. *J. Am. Chem. Soc.* **2001**, *123*, 4181-4188. (b) Lee, M. D.; Dennis, M. L.; Swarbrick, J. D.; Graham, B. Enantiometric Two-armed Lanthanide-binding Tags for Complementary Effects in Paramagnetic NMR Spectroscopy. *Chem. Commun.* **2016**, *52*, 7954-7957. (c) Graham, B.; Loh, C. T.; Swarbrick, J. D.; Ung, P.; Shin, J.; Yagi, H.; Xinying, J.; Chhabra, S.; Barlow, N.; Pintacuda, G.; Huber, T.; Otting, G. DOTA-Amide Lanthanide Tag for Reliable Generation of Pseudocontact Shifts in Protein NMR Spectra. *Bioconjugate Chem.* **2011**, *22*, 2118-2125.

(13) Pedersen, K. S.; Dreiser, J.; Weihe, H.; Sibille, R.; Johannesen, H. V.; Sorensen, M. A.; Nielsen, B. E.; Sigrist, M.; Mutka, H.; Rols, S.; Bendix, J.; Piligkos, S. Design of Single-Molecule Magnets: Insufficiency of the Anisotropy Barrier as the Sole Criterion. *Inorg. Chem.* **2015**, *54*, 7600-7606.

(14) (a) Lelli, M.; Pintacuda, G.; Cuzzola, A.; Di Bari, L. Monitoring Proton Dissociation and Solution Conformation of Chiral Ytterbium Complexes with Near-IR CD. *Chirality* **2005**, *17*, 201-211. (b) Di Bari, L.; Pintacuda, G.; Salvadori, P.; Dickins, R.; Parker, D. Effect of Axial Ligation on the Magnetic and Electronic Properties of Lanthanide Complexes of Octadentate Ligands. *J. Am. Chem. Soc.* **2000**, *122*, 9257-9264. (c) Di Bari, L.; Pescitelli, G.; Sherry, A. D.; Woods, M. Structural and Chiroptical Properties of the Two Coordination Isomers of YbDOTA-Type Complexes. *Inorg. Chem.* **2005**, *44*, 8391-8398.

(15) (a) Ouali, N.; Bocquet, B.; Rigault, S.; Morgantini, P.-Y.; Weber, J.; Piguet, C. Analysis of Paramagnetic NMR Spectra of Triple Helical Lanthanide Complexes with 2,6-Dipicolinic Acid Revisited: A New Assignment of Structural Changes and Crystal-Field Effects 25 Years Later. *Inorg. Chem.* **2002**, *41*, 1436-1445. (b) Brayshaw, P. A.; Bünzli, J.-C. G.; Froidevaux, P.; Harrowfield, J. M.; Kim, Y.; Sobolev, A. N. Synthetic, Structural, and Spectroscopic Studies on Solids Containing Tris(dipico1inato) Rare Earth Anions and Transition or Main Group Metal Cations. *Inorg. Chem.* **1995**, *34*, 2068-2076.

(16) Kervern, G.; D'Aléo, A.; Toupet, L.; Maury, O.; Emsley, L.; Pintacuda, G. Crystal-Structure Determination of Powdered Paramagnetic Lanthanide Complexes by Proton NMR Spectroscopy. *Angew. Chem. Int. Ed.* **2009**, *48*, 3082-3086.

(17) (a) Castro, G.; Regueiro-Figueroa, M.; Esteban-Gómez, D.; Bastida, R.; Macías, A.; Pérez-Lourido, P.; Platas-Iglesias, C.; Valencia, L. Exceptionally Inert Lanthanide(III) PARACEST MRI Contrast Agents Based on an 18-Membered Macrocyclic Platform. *Chem. Eur. J.* **2015**, *21*, 18662-18670; (b) Castro, G.; Regueiro-Figueroa, M.; Esteban-Gómez, D.; A.; Pérez-Lourido, P.; Platas-Iglesias, C.; Valencia, L. Magnetic Anisotropies in Rhombic Lanthanide(III) Complexes Do Not Conform to Bleaney's Theory. *Inorg. Chem.* **2016**, *55*, 3490-3497.

(18) (a) Rodríguez-Rodríguez, A.; Esteban-Gómez, D.; de Blas, A.; Rodríguez-Blas, T.; Fekete, M.; Botta, M.; Tripier, R.; Platas-Iglesias, C. Lanthanide Complexes with Ligands Derived from a Cyclen Framework Containing Pyridinecarboxylate Pendants. The Effect of Steric Hindrance on the Hydration Number. *Inorg. Chem.* **2012**, *51*, 2509-2521; (b) Rodríguez-Rodríguez, A.; Esteban-Gómez, D.; de Blas, A.; Rodríguez-Blas, Botta, M.; Tripier, R.; Platas-Iglesias, C. Solution Structure of Ln(III) Complexes with Macrocyclic Ligands Through Theoretical Evaluation of ^{1}H NMR Contact Shifts. *Inorg. Chem.* **2012**, *51*, 13419-13429.

(19) Aravena, D.; Atanasov, M.; Neese, F. Periodic Trends in Lanthanide Compounds through the Eyes of Multireference ab Initio Theory. *Inorg. Chem.* **2016**, *55*, 4457-4469.

(20) (a) Esteban-Gomez, D.; de Blas, A.; Rodriguez-Blas, T.; Helm, L.; Platas-Iglesias, C. Hyperfine Coupling Constants on Inner-Sphere Water Molecules of Gd^{III}-Based MRI Contrast Agents. *ChemPhysChem*, **2012**, *13*, 3640-3650. (b) Regueiro-Figueroa, M.; Platas-Iglesias, C. Toward the Prediction of Water Exchange Rates in Magnetic Resonance Imaging Contrast Agents: A Density Functional Theory Study. *J. Phys. Chem. A* **2015**, *119*, 6436-6445.

(21) (a) Forsberg, J. H.; Delaney, R. M.; Zhao, Q.; Harakas, G.; Chandran, R. Analyzing Lanthanide-Induced Shifts in the NMR Spectra of Lanthanide(III) Complexes Derived from 1,4,7,10-Tetrakis(N,N-diethylacetamido)-l,4,7,l0-tetraazacyclododecane. *Inorg. Chem.* **1995**, *34*, 3705-3715. (b) Bertini, I.; Luchinat, C.; Parigi, G. Magnetic Susceptibility in Paramagnetic NMR. *Prog. Nucl. Magn. Reson. Spectrosc.* **2002**, *40*, 249-273.

(22) Su, X.-C.; Liang, H.; Loscha, K. V.; Otting, G. $[Ln(DPA)_3]^{3-}$ Is a Convenient Paramagnetic Shift Reagent for Protein NMR Studies. *J. Am. Chem. Soc.* **2009**, *131*, 10352-10353.

(23) Mason, K.; Harnden, A. C.; Patrick, C. W.; Poh, A. W. J.; Batnasov, A. S.; Suturina, E. A.; Vonci, M.; McInnes, E. J. L.; Chilton, N. F.; Parker, D. Exquisite Sensitivity of the Ligand Field to Solvation and Donor Polarisability in Coordinatively Saturated Lanthanide Complexes. *Chem. Commun.* **2018**, *54*, 8486-8489.

(24) Funk, A. M.; Finney, K.-L. N. A.; Harvey, P.; Kenwright, A. M.; Neil, E. R.; Rogers, N. J.; Senanayake, P. K.; Parker, D. Critical analysis of the limitations of Bleaney's theory of magnetic anisotropy in paramagnetic lanthanide coordination complexes. *Chem. Sci.* **2015**, *6*, 1655-1662.

(25) Driesen, K.; Van Deun, R.; Görller-Walrand, C.; Binnemans, K. Near-Infrared Luminescence of Lanthanide Calcein and Lanthanide Dipicolinate Complexes Doped into a Silica-PEG Hybrid Material. *Chem. Mater.* **2004**, *16*, 1531-1535.

(26) Moore, E. G.; Grilj, J.; Vauthey, E.; Ceroni, P. A comparison of sensitized Ln(III) emission using pyridine- and pyrazine-2,6-dicarboxylates – part II. *Dalton Trans.* **2013**, *42*, 2075-2083.

(27) Asano-Someda, M.; Kaizu, Y. Hot bands of (f, f*) emission from ytterbium(III) porphyrins in solution. *J. Photochem. Photobiol. A Chem.* **2001**, *139*, 161-165.

(28) Goldner, Ph.; Pellé, F.; Meichenin, D.; Auzel, F. Cooperative Luminescence in Ytterbium-doped $CsCdBr_3$. *J. Lumin.* **1997**, *71*, 137-150.

(29) Demchenko, A. P.; Tomin, V. I.; Chou, P.-T. Breaking the Kasha Rule for More Efficient Photochemistry. *Chem. Rev.* **2017**, *117*, 13353−13381.

(30) Rafizadeh, M.; Ranjbar, M.; Amani, V. Dihydronium 2,6-Diaminopyridinium Tris(2,6-pyridinedicarboxylato)ytterbate(III) Dihydrate. *Acta Cryst.* **2004**, *E60*, m479-m481.

(31) Nonat, A.; Bahamyirou, S.; Lecointre, A.; Przybilla, F.; Mély, Y.; Platas-Iglesias, C.; Camerel, F.; Jeannin, O.; Charbonniére, L. Molecular Upconversion in Water in Heteropolynuclear Supramolecular Tb/Yb Assemblies. *J. Am. Chem. Soc.* Submitted.

(32) Ruíz-Martínez, A.; Casanova, D.; Álvarez, S. Polyhedral Structures with an Odd Number of Vertices: Nine-Coordinate Metal Compounds. *Chem Eur. J.* **2008**, *14*, 1291-1303.

(33) (a) Atanasov, M.; Ganyushin, D.; Sivalingam, K.; Neese, F. Molecular Electronic Structures of Transition Metal Complexes II. In Structure and Bonding; Mingos, D. M. P., Day, P., Dahl, J. P., Eds.; Springer: Berlin, Germany, 2012; Vol. 143, pp 149−220; (b) Atanasov M.; Aravena, D.; Suturina, E.; Bill, E.; Maganas, D.; Neese, F. First principles approach to theelectronic structure, magnetic anisotropy and spin relaxation in mononuclear 3d-transition metal single molecule magnets. *Coord. Chem. Rev.* **2015**, *289*, 177-214.

(34) Jung, J.; Atanasov, M.; Neese, F. Ab Initio Ligand-Field Theory Analysis and Covalency Trends in Actinide and Lanthanide Free Ions and Octahedral Complexes. *Inorg. Chem.* **2017**, *56*, 8802-8816.

(35) (a) Khan, S.; Kubica-Misztal, A.; Kruk, D.; Kowalewski, J.; Odelius, M. Systematic Theoretical Investigation of the Zero-Field Splitting in Gd(III) Complexes: Wave Function and Density Functional Approaches. *J. Chem. Phys.* **2015**, *142*, 034304. (b) Freidzon, A. Y.; Kurchatov, I. A.; Vovna, V. I. Ab Initio Calculations of Energy Levels of Trivalent Lanthanide Ions. *Phys. Chem. Chem. Phys.* **2018**, *20*, 14564-14577. (c) Khan, S.; Pollet, R.; Vuilleumier, R.; Kowalewski, J.; Odelius, M. An ab initio CASSCF Study of Zero Field Splitting Fluctuations in the Octet Ground State of Aqueous [Gd(III)(HPDO3A)(H_2O)]. *J. Chem. Phys.* **2017**, *147*, 244306. (d) Janicki, R.; Kedziorski, A.; Mondry, A. The First Example of Ab Initio Calculations of f-f Transitions for the case of [Eu(DOTP)]$^{5-}$ Complex-Experiment versus Theory. *Phys. Chem. Chem. Phys.* **2016**, *18*, 27808-27817. (e) Oyarzabal, I.; Ruiz, J.; Seco, J. M.; Evangelisti, M.; Camon, A.; Ruiz, E.; Aravena, D.; Colacio, E. Rational Electrostatic Design of Easy-Axis Magnetic Anisotropy in a Zn^{II}–Dy^{III}–Zn^{II} Single-Molecule Magnet with a High Energy Barrier. *Chem. Eur. J.* **2014**, *20*, 14262-14269. (f) Goodwin, C. A. P.; Reta, D.; Ortu, F.; Chilton, N. F.; Mills, D. P. Synthesis and Electronic Structures of Heavy Lanthanide Metallocenium Cations. *J. Am. Chem. Soc.* **2017**, *139*, 18714-18724.

(36) Frisch, M. J.; Gaussian09, revision D.01; Gaussian, Inc.: Wallingford, CT, 2010.

(37) Tao, J. M.; Perdew, J. P.; Staroverov, V. N.; Scuseria, G. E. Climbing the Density Functional Ladder: Nonempirical Meta-Generalized Gradient Approximation Designed for Molecules and Solids. *Phys. Rev. Lett.* **2003**, *91*, 146401.

(38) Dolg, M.; Stoll, H.; Savin, A.; Preuss, H. Energy-adjusted pseudopotentials for the rare earth elements. *Theor. Chim. Acta* **1989**, *75*, 173-194.

(39) Malqvist, P.-A.; Roos, B. O. The CASSCF State Interaction Method. *Chem. Phys. Lett.* **1989**, *155*, 189-194.

(40) (a) Angeli, C.; Cimiraglia, R.; Malrieu, J.-P. N-Electron Valence State Perturbation Theory: A Fast Implementation of the Strongly Contracted Variant. *Chem. Phys. Lett.* **2001**, *350*, 297–305. (b) Angeli, C.; Cimiraglia, R.; Malrieu, J.-P. N-Electron Valence State Perturbation Theory: A Spinless Formulation and an Efficient Implementation of the Strongly Contracted and of the Partially Contracted Variants. *J. Chem. Phys.* **2002**, *117*, 9138–9153. (c) Angeli, C.; Cimiraglia, R.; Evangelisti, S.; Leininger, T.; Malrieu, J.-P.; Introduction of N-Electron Valence States for Multireference Perturbation Theory. *J. Chem. Phys.* **2001**, *114*, 10252–10264. (d) Angeli, C.; Cimiraglia, R. Multireference Perturbation Configuration Interaction V. Third-order Energy Contributions in the Moller-Plesset and Epstein-Nesbet Partitions. *Theor. Chem. Acc.* **2002**, *107*, 313–317.

(41) (a) Neese, F. The ORCA program system, *WIREs Comput. Mol. Sci.* **2012**, *2*, 73-78; (b) Neese, F. Software Update: The ORCA Program System, version 4.0. *WIREs Comput. Mol. Sci.* **2018**, *8*, e1327.

(42) (a) Barysz, M.; Sadlej, A. J. Two-component methods of relativistic quantum chemistry: from the Douglas-Kroll approximation to the exact two-component formalism. *J. Mol. Struct. (Theochem)* **2001**, *573*, 181-200. (b) Reiher, M. Douglas-Kroll-Hess Theory: A Relativistic Electrons-Only Theory for Chemistry. *Theor. Chem. Acc.* **2006**, *116*, 241-252.

(43) Aravena, D.; Neese, F.; Panzatis, D. A. Improved Segmented All-Electron Relativistically Contracted Basis Sets for the Lanthanides. *J. Chem. Theory Comput.* **2016**, *12*, 1148-1156.

(44) Weigend, F.; Ahlrichs, R. Balanced Basis Sets of Split Valence, Triple Zeta Valence and Quadruple Zeta Valence Quality for H to Rn: Design and Assessment of Accuracy. *Phys. Chem. Chem. Phys.* **2005**, *7*, 3297-3305.

(45) Pantazis, D. A.; Chen, X.-Y.; Landis, C. R.; Neese, F. All-Electron Scalar Relativistic Basis Sets for Third-Row Transition Metal Atoms. *J. Chem. Theory Comput.* **2008**, *4*, 908-919.

(46) (a) Neese, F.; Wennmohs, F.; Hansen, A.; Becker, U. Efficient, Approximate and Parallel Hartree–Fock and Hybrid DFT Calculations. A 'Chain-of-Spheres' Algorithm for the Hartree–Fock Exchange. *Chem. Phys.* **2009**, *356*, 98-109. (b) Izsak, R.; Neese, F. An Overlap Fitted Chain of Spheres Exchange Method. *J. Chem. Phys.* **2011**, *135*, 144105. (c) Petrenko, T.; Kossmann, S.; Neese, F. Efficient Time-Dependent Density Functional Theory Approximations for Hybrid Density Functionals: Analytical Gradients and Parallelization. *J. Chem. Phys.* **2011**, *134*, 054116. (d) Kossmann, S.; Neese, F. Comparison of Two Efficient Approximate Hartree-Fock Approaches. *Chem. Phys. Lett.* **2009**, *481*, 240-243.

(47) Stoychev, G. L.; Auer, A. A.; Neese, F. Automatic Generation of Auxiliary Basis Sets. *J. Chem. Theory Comput.* **2017**, *13*, 554-562.

(48) Neese, F. Efficient and Accurate Approximations to the Molecular Spin-Orbit Coupling Operator and Their Use in Molecular g-Tensor Calculations. *J. Chem. Phys.* **2005**, *122*, 034107.

(49) Marenich, A. V.; Cramer, C. J.; Truhlar, D. G. Universal Solvation Model Based on Solute Electron Density and on a Continuum Model of the Solvent Defined by the Bulk Dielectric Constant and Atomic Surface Tensions. *J. Phys. Chem. B* **2009**, *113*, 6378-6396.

(50) Gorelsky, S. I.; Lever, A. B. P. Electronic structure and spectra of ruthenium diimine complexes by density functional theory and INDO/S. Comparison of the two methods. *J. Organometal. Chem.* **2001**, *635*, 187-196.